

## Sub-nanoscale Surface Engineering of TiO<sub>2</sub> Nanoparticles by Molecular Layer Deposition of Poly(ethylene terephthalate) for Suppressing Photoactivity and Enhancing Dispersibility

La Zara, Damiano; Bailey, Maximilian R.; Hagedoorn, Peter Leon; Benz, Dominik; Quayle, Michael J.; Folestad, Staffan; Van Ommen, J. Ruud

**DOI**

[10.1021/acsnm.0c01158](https://doi.org/10.1021/acsnm.0c01158)

**Publication date**

2020

**Document Version**

Final published version

**Published in**

ACS Applied Nano Materials

**Citation (APA)**

La Zara, D., Bailey, M. R., Hagedoorn, P. L., Benz, D., Quayle, M. J., Folestad, S., & Van Ommen, J. R. (2020). Sub-nanoscale Surface Engineering of TiO<sub>2</sub> Nanoparticles by Molecular Layer Deposition of Poly(ethylene terephthalate) for Suppressing Photoactivity and Enhancing Dispersibility. *ACS Applied Nano Materials*, 3(7), 6737-6748. <https://doi.org/10.1021/acsnm.0c01158>

**Important note**

To cite this publication, please use the final published version (if applicable). Please check the document version above.

**Copyright**

Other than for strictly personal use, it is not permitted to download, forward or distribute the text or part of it, without the consent of the author(s) and/or copyright holder(s), unless the work is under an open content license such as Creative Commons.

**Takedown policy**

Please contact us and provide details if you believe this document breaches copyrights. We will remove access to the work immediately and investigate your claim.

# Sub-nanoscale Surface Engineering of TiO<sub>2</sub> Nanoparticles by Molecular Layer Deposition of Poly(ethylene terephthalate) for Suppressing Photoactivity and Enhancing Dispersibility

Damiano La Zara,<sup>\*,†</sup> Maximilian R. Bailey,<sup>†</sup> Peter-Leon Hagedoorn, Dominik Benz, Michael J. Quayle, Staffan Folestad, and J. Ruud van Ommen



Cite This: *ACS Appl. Nano Mater.* 2020, 3, 6737–6748



Read Online

ACCESS |



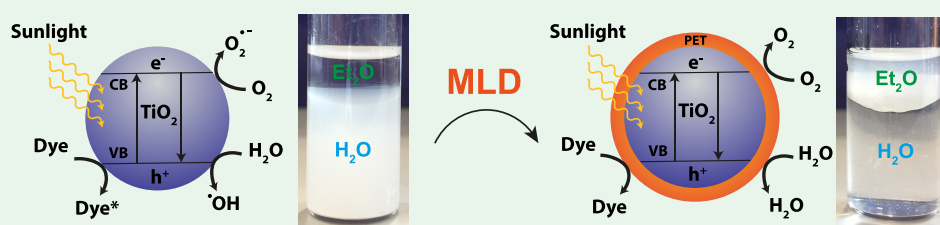
Metrics & More



Article Recommendations



Supporting Information



**ABSTRACT:** In this work, we report molecular layer deposition (MLD) of ultrathin poly(ethylene terephthalate) (PET) films on gram-scale batches of ultrafine particles for the first time. TiO<sub>2</sub> P25 nanoparticles (NPs) are coated up to 50 cycles in an atmospheric-pressure fluidized-bed reactor at ~150 °C using terephthaloyl chloride and ethylene glycol as precursors. Ex-situ diffuse reflectance infrared Fourier transform spectroscopy, thermogravimetric analysis, and transmission electron microscopy show the linear growth at ~0.05 nm/cycle of uniform and conformal PET films, which are unattainable with conventional wet-phase approaches. The sub-nanoscale and nanoscale PET films not only suppress the photocatalytic activity of TiO<sub>2</sub> NPs by hindering the access of water and reactant molecules to the TiO<sub>2</sub> surface but also improve the dispersibility of TiO<sub>2</sub> NPs in both organic and aqueous media. Still, the bulk optical properties, electronic structure, and surface area of TiO<sub>2</sub> are essentially unaffected by the MLD process. This study demonstrates the industrial relevance of MLD to simultaneously suppress the photoactivity and enhance the dispersibility of commercial TiO<sub>2</sub> P25 nanopowders, which is crucial for their use for example as UV-screening agents in sunscreens and as white pigments in paints. Moreover, by rapidly modifying the surface properties of particles in a controlled manner at the sub-nanometer scale, particle MLD can serve many other applications ranging from nanofluids to emulsions to polymer nanocomposites.

**KEYWORDS:** molecular layer deposition, sub-nanoscale, surface engineering, organic coating, polyethylene terephthalate, TiO<sub>2</sub>, inorganic–organic nanocomposite, suppressed photoactivity, improved dispersion

## INTRODUCTION

Nanoscale coatings have received considerable interest for their ability to modify the surface properties of various functional materials, without altering their bulk properties. Emergent functionalities such as enhanced mechanical, thermal, and chemical properties; tailored wettability; electrical conductivity; and transparency can arise from the confinement of the coating thickness to the nanoscale.<sup>1</sup> As a subset of ultrathin films, sub-nanoscale coatings promise to advance the benefits provided by nanoscale films.<sup>2</sup> Sub-nanofilms allow a more efficient use of resources and do not affect the geometry of even high-aspect-ratio nanostructured substrate materials.<sup>3</sup> Furthermore, the controlled growth of sub-nanofilms may allow the fabrication of novel materials with unprecedented properties for several potential applications in energy conversions such as electrocatalysis and photocatalysis.<sup>4</sup>

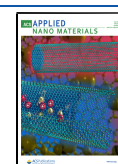
Surface passivation by ultrathin films is another area of active research, as demonstrated by the considerable attention given

to suppressing the photocatalytic activity of nanoscale TiO<sub>2</sub> for its use in commercial products such as sunscreens and paints.<sup>5–7</sup> TiO<sub>2</sub> can act as an effective UV-screening agent thanks to its ability to absorb in the UV spectrum. Moreover, the high efficiency with which TiO<sub>2</sub> scatters visible light makes it an excellent bright white pigment for the paints and coatings industries. However, the high photocatalytic activity of TiO<sub>2</sub> under UV light causes the generation of radical species which can degrade organic binders in paints,<sup>8</sup> thus reducing the product lifetime. Such radical species are also undesirable in cosmetics due to increasing concerns of potential carcinogenic

Received: April 28, 2020

Accepted: June 5, 2020

Published: June 5, 2020



effects.<sup>9</sup> Therefore, to prevent the photodegradation of TiO<sub>2</sub>-based products, TiO<sub>2</sub> particles are typically coated with ultrathin inorganic films such as Al<sub>2</sub>O<sub>3</sub> and SiO<sub>2</sub>,<sup>10,11</sup> which can block the transport of electrons and holes generated by UV-light absorption to the surface, without deteriorating the white pigmentation.

Organic coatings are of increasing interest for this photosuppressive effect<sup>5,6,12</sup> due to the advantages they hold over their inorganic analogues, such as biocompatibility,<sup>13,14</sup> lower raw material costs, and reduced environmental impact.<sup>15</sup> In industry, the biocompatibility of polymeric films is of particular interest to the cosmetics sector<sup>7,16</sup> and promises applicability to nanomedicine.<sup>17</sup> Organic coatings also provide the opportunity to improve particle dispersibility in organic media,<sup>18,19</sup> potentially enhancing the performance of organic-based paints, nanofluids,<sup>20</sup> Pickering emulsions,<sup>21</sup> and polymer nanocomposites.<sup>22</sup>

Typically, organic coatings are synthesized via wet-phase techniques.<sup>5–7,18,19,23,24</sup> Liquid-based approaches are well-established, offering versatility and a large degree of control over experimental conditions. However, they provide non-conformal coverage and often produce excessive amounts of waste.<sup>25,26</sup> Moreover, the requirement for multiple, at times complex, synthesis steps as well as further postprocessing separation and drying stages is undesirable.<sup>27</sup> Vapor-phase approaches remove these steps, thereby eliminating solvent damage to substrates and reducing the introduction of contaminants.<sup>28</sup> Chemical vapor deposition (CVD) is the most widespread vapor-phase coating process, in which typically two monomers are introduced simultaneously, thus enabling concurrent polymerization and thin film deposition.<sup>29,30</sup> However, CVD coatings, especially on high-aspect-ratio substrates, are typically nonconformal, thus providing incomplete surface passivation and modification. Therefore, thicker films than desired are often produced to ensure complete surface coverage, consequently altering surface morphology, and increasing raw material inputs and costs.<sup>31</sup> Alternating vapor deposition polymerization (VDP) was thus developed to provide greater control over film growth by introducing monomers alternatively to the reaction chamber.<sup>32</sup> Although the control provided by VDP is superior to that of CVD, unreacted gaseous monomers which remain present in the chamber will still react with subsequently introduced monomers, preventing the degree of fine control necessary for sub-nanocoatings and low-nanocoatings.<sup>33</sup>

The shortcomings of the above-mentioned processes have led to the development of molecular layer deposition (MLD) to achieve the controlled growth of ultrathin films. Like VDP, MLD involves the cyclical introduction of gaseous monomer precursors into the reaction chamber. However, in MLD each monomer pulse is separated by a purge step with an inert gas, minimizing uncontrolled CVD-type growth. Pure MLD, which is the organic analogue of atomic layer deposition (ALD), was first demonstrated by Yoshimura et al., who deposited thin films of polyimides in the 1990s.<sup>34</sup> The consecutive, self-limiting chemical reactions between the substrate surface and the gaseous precursors enable the controlled, layer-by-layer growth of conformal polymeric coatings on a range of materials.<sup>35</sup> This degree of control is promising for both electronic and biomedical applications, especially when considering the ability to impart films with a wide range of functionalities by appropriately selecting the organic precursors.<sup>33,36,37</sup> Nevertheless, despite this potential for surface

modification at the nanoscale, only limited research has been devoted to pure organic MLD compared to ALD and even hybrid ALD/MLD processes.<sup>37–39</sup> Moreover, the conformal (sub)nano surface engineering of gram-scale fine primary particles by pure MLD for industrially relevant applications has not yet been demonstrated.

In this work, we report MLD of sub-nanoscale and nanoscale polyethylene terephthalate (PET) films to tailor the photoactivity and dispersibility of gram-scale batches of TiO<sub>2</sub> P25 nanoparticles (NPs). The MLD growth characteristics were examined by ex-situ diffuse reflectance infrared Fourier transform spectroscopy (DRIFTS), thermogravimetric analysis (TGA), and transmission electron microscopy (TEM). X-ray photoelectron spectroscopy (XPS) measurements were also performed to further study the PET film composition and electronic structure of TiO<sub>2</sub>. The growth per cycle (GPC) on fluidized TiO<sub>2</sub> P25, measured by TEM analysis, was then compared to the GPC determined by spectroscopic ellipsometry on flat Si wafers. UV photocatalytic dye degradation and methanol oxidation tests were performed to determine the efficacy of the PET films in suppressing the photoactivity of TiO<sub>2</sub> P25. To probe the mechanism by which the PET film alters the photocatalytic properties of the TiO<sub>2</sub> NPs, UV–vis diffuse reflectance spectroscopy (UV-DRS), BET adsorption isotherms, and electron paramagnetic resonance (EPR) measurements were then taken. The ability of the PET films to modify particle dispersion in both aqueous and organic media was finally investigated by zeta potential analysis and by the use of apolar solvent–water mixtures, respectively.

## ■ EXPERIMENTAL SECTION

**Materials.** The MLD precursors, terephthaloyl chloride (TC) and ethylene glycol (EG), were purchased from Sigma-Aldrich and used as received. Both precursors were stored in stainless steel bubblers under an inert atmosphere. Aeroxide P25 titanium dioxide nanoparticles (primary particle size of 21 nm and specific surface area of ~52 m<sup>2</sup>/g) were provided by Evonik and used as a substrate for the deposition. Powders were sieved at 150 μm before use to remove the large agglomerates.

**MLD Experiments.** The MLD experiments were carried out in a custom-built fluidized-bed reactor operating at atmospheric pressure (Figure 1), as described elsewhere.<sup>40</sup> The system consists of a glass column (internal diameter of 2.5 cm and height of 50 cm) resting on a double motor Paja PTL 40/40-24 vibration table to assist fluidization of the TiO<sub>2</sub> nanoparticles. Two stainless steel distributor plates were placed at the bottom and the top of the column to ensure a homogeneous gas distribution and to prevent any powder loss from the reactor, respectively. The TC and EG precursors were contained within separate stainless steel bubblers under an inert atmosphere and heated to 100 and 105 °C, respectively, with the aid of a heating tape. Precursors were delivered to the reactor by flowing N<sub>2</sub> (99.999 v/v%) gas through the bubblers. Three separate gas lines were connected to the reactor: two for precursor delivery, and one for the purge N<sub>2</sub> gas. This design minimizes the risk of contamination and prevents unwanted CVD reactions within the lines. The lines were kept at 30 °C above the bubbler temperature by using heating tapes to prevent condensation and underdelivery of precursors. The reactor was maintained at a temperature of 150 °C by using a feedback-controlled infrared lamp, placed parallel to the column. The temperature inside the fluidized powder bed was monitored with a type-K thermocouple inserted into the column. The off-gas of the fluidized bed was led through a series of washing bubblers containing mineral oil (Kaydol) to trap unreacted precursors and reaction byproducts, and NaOH solution to neutralize chloride compounds arising from TC. The precursor bubblers, the lines, the reactor, and the washing bottles were contained inside a closed cabinet. In each experiment, 1.5 g of

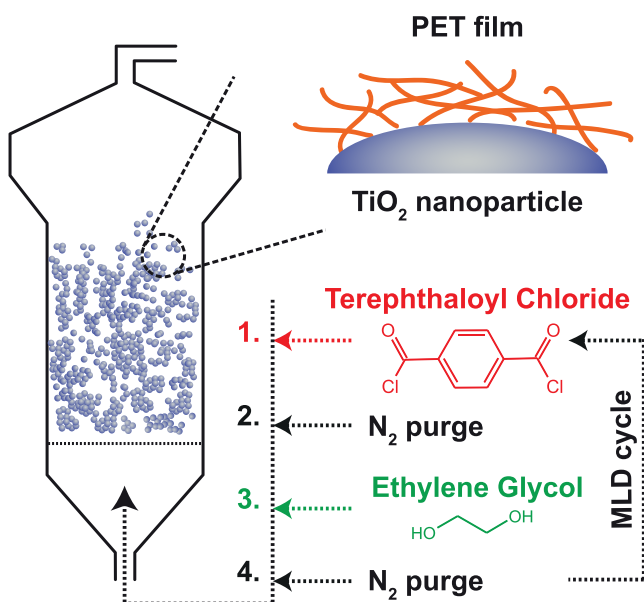


**Figure 1.** Fluidized-bed molecular layer deposition of polyethylene terephthalate films on  $\text{TiO}_2$  nanoparticles. The orange filaments indicate PET oligomers made of monomers of terephthaloyl chloride and ethylene glycol.

$\text{TiO}_2$  powder was used. Prior to use, the powder was dried at  $120^\circ\text{C}$  overnight. An optimized gas flow of  $0.5\text{ NL min}^{-1}$  was introduced at the bottom of the reactor column to fluidize the powder. One complete MLD cycle consisted of sequential exposures of the powder to TC (1 min) and EG (1 min), separated by  $\text{N}_2$  purging steps (5 min).

**Material Characterization.** The mass of the PET coating was quantified by thermogravimetric analysis using the TGA/SF1100 STARE system (Mettler Toledo). For this analysis, samples in the range 7–12 mg were prepared. Thermogravimetric curves were recorded while the powders were heated from  $25$  to  $800^\circ\text{C}$ , with a ramping rate of  $5^\circ\text{C min}^{-1}$  in a synthetic air flow of  $100\text{ mL min}^{-1}$ . The PET loadings were calculated taking into account the weight loss of the samples between  $225$  and  $450^\circ\text{C}$  due to PET ( $W_{\text{PET}/\text{TiO}_2,225-450^\circ\text{C}}$ ) and the specific surface area (SSA) of the  $\text{TiO}_2$  nanoparticles, according to eq 1:

$$\text{PET loading} = \frac{W_{\text{PET}/\text{TiO}_2,225-450^\circ\text{C}} \times 1000}{(1 - W_{\text{PET}/\text{TiO}_2,225-450^\circ\text{C}}) \times \text{SSA}} \frac{\text{mg}}{\text{m}^2} \quad (1)$$

The thickness of the PET film ( $t_{\text{PET}}$ ) resulting from the PET wt % ( $x_{\text{PET}}$ ) was calculated according to the equation described by Zhang et al.<sup>41</sup> correlating the mass fraction and the thickness of the deposited material, assuming a  $\text{TiO}_2$  particle diameter ( $d_{\text{TiO}_2}$ ) of  $32.7\text{ nm}$  ( $d_{3,2}$ ),<sup>42</sup> a  $\text{TiO}_2$  density ( $\rho_{\text{TiO}_2}$ ) of  $4.23\text{ g/cm}^3$ , and a PET density ( $\rho_{\text{PET}}$ ) of  $1.38\text{ g/cm}^3$ , typical of bulk PET (eq 2):

$$t_{\text{PET}} = \frac{d_{\text{TiO}_2}}{2} \left( \sqrt[3]{\frac{x_{\text{PET}} \rho_{\text{TiO}_2}}{1 - x_{\text{PET}} \rho_{\text{PET}}} + 1} - 1 \right) \quad (2)$$

The characteristic features of the PET films were observed by ex-situ diffuse reflectance infrared Fourier transform spectroscopy. The analyses were conducted in diffuse reflectance mode using a Nicolet 8700 spectrometer (Thermo Fisher Scientific) equipped with a deuterated triglycine sulfate (DTGS) detector. The measurements were performed at room temperature with a freshly prepared KBr sample (>99%, FTIR grade, Harrick Scientific Corporation) as background. Spectra were recorded from  $4000$  to  $400\text{ cm}^{-1}$  and averaged over 128 scans, using a resolution of  $4.0\text{ cm}^{-1}$ . The spectra were then analyzed with OMNIC 8.0 software (Thermo Fisher

Scientific). The spectrum of bare  $\text{TiO}_2$  recorded on the same day was subtracted from the spectra of the coated  $\text{TiO}_2$ . The resulting spectra were converted to Kubelka–Munk units for quantitative analysis using OMNIC built-in functions. The integrated area of the ester carbonyl peak, centered at  $1725\text{ cm}^{-1}$ , was then evaluated using the peak area tool on OMNIC, which automatically determines an appropriate baseline for the region of interest. To estimate the error inherent to this analytical approach, DRIFTS spectra of each sample were measured on 3 different days.

The presence of PET coatings on the  $\text{TiO}_2$  P25 NPs was verified with transmission electron microscopy. Samples were prepared by dispersing the dry coated powders on copper TEM grids of  $3.05\text{ mm}$  in diameter. TEM images were recorded at various locations on the grid using a JEOL JEM-1400 electron microscope operating at  $120\text{ kV}$ . The thickness of the PET films was evaluated with ImageJ software. For each sample, the film thickness of about 10 particle agglomerates was measured at multiple locations and averaged.

Spectroscopic ellipsometry measurements were obtained with a commercial ellipsometer (M-2000F, J.A. Woollam Co. Inc.). Data fitting was performed using WVASE spectroscopic ellipsometry data acquisition and analysis software.

X-ray photoelectron spectroscopy measurements were carried out using a ThermoFisher K-Alpha system (ThermoFisher Scientific) using  $\text{Al K}\alpha$  radiation with photon energy of  $1486.7\text{ eV}$ . A few milligrams of powder was immobilized on carbon tape before loading into the XPS chamber. Survey scans were acquired using a  $200\text{ }\mu\text{m}$  spot size,  $55\text{ eV}$  pass energy, and  $0.1\text{ eV/step}$  with charge neutralization. The peaks positions were calibrated according to the C 1s peak at  $284.8\text{ eV}$  using the CasaXPS software.

The photocatalytic tests of Acid Blue 9 (AB9) degradation and methanol (MeOH) oxidation were performed in a Atlas Suntest XXL + sun simulator using Xe lamps ( $300\text{--}400\text{ nm}$ ,  $45\text{ W/m}^2$ ). For the AB9 degradation,  $16\text{ mg/mL}$  of AB9 dye were placed in  $30\text{ mL}$  of demineralized water with  $1\text{ mg/mL}$  of  $\text{TiO}_2$ . Similarly, for MeOH oxidation,  $30\text{ mL}$  of  $100\text{ mM}$  methanol aqueous solution ( $0.12\text{ mL}$  methanol in  $30\text{ mL}$  demineralized water) was prepared with  $1\text{ mg/mL}$  of  $\text{TiO}_2$ . Each aqueous solution thus contained  $30\text{ mg}$  of  $\text{TiO}_2$ , even in the case of the PET-coated samples. More precisely,  $30\text{ mg}$  of bare  $\text{TiO}_2$ ,  $31\text{ mg}$  of 10-cycle-PET-coated  $\text{TiO}_2$ ,  $32.3\text{ mg}$  of 25-cycle-PET-coated  $\text{TiO}_2$ , and  $34.7\text{ mg}$  of 50-cycle-PET-coated  $\text{TiO}_2$  were used to compensate for the PET mass and thus ensure the same  $\text{TiO}_2$  mass in each photocatalytic test. The solutions were agitated through an RO 15 power IKAMAG(R) magnetic stirring plate with 15 different stirring positions to maintain a well-mixed dispersion. The temperature was maintained at  $20^\circ\text{C}$  using a Watson Marlow 323 pump and a Julabo FL300 temperature control unit. The  $t = 0$  measurements were taken after 10 min of sonication and 20 min of stirring without irradiation to attain equilibrium adsorption. The solutions were then irradiated continuously for 50 min, with  $1\text{ mL}$  aliquots removed at predetermined time intervals ( $t = 5, 10, 15, 20, 30, 40, 50\text{ min}$ ). The  $1\text{ mL}$  AB9 samples were directly centrifuged to separate from the nanoparticles and then measured by UV–vis absorption, whereas the  $1\text{ mL}$  formaldehyde ( $\text{CH}_2\text{O}$ ) samples were first mixed with  $1\text{ mL}$  of a  $0.18\text{ M}$  ammonium dihydrogen phosphate buffer solution ( $\text{pH} = 6.0$ , adjusted with  $\text{NH}_3$ ) and  $20\text{ }\mu\text{L}$  of acetylacetone. The formation of  $\text{CH}_2\text{O}$  can be analyzed by colorimetry using the Nash method, which is based on the reaction of  $\text{CH}_2\text{O}$  with ammonium phosphate and acetylacetone to form a colored a product with a maximum absorption at  $412\text{ nm}$ . The samples were later centrifuged twice for 10 min at  $12\,500\text{ rpm}$  in a Thermo Scientific MicroCL 21R. After each centrifugation cycle, the supernatant was removed ( $0.8\text{ mL}$  after the first cycle and  $0.4\text{ mL}$  after the second cycle) to separate the nanoparticles present in solution. The UV–vis absorption spectra of both the AB9 and  $\text{CH}_2\text{O}$  solutions were taken in a HACH LANGE DR 5000TM UV–vis spectrophotometer, and concentrations were evaluated at the absorption peak of  $629\text{ nm}$  for AB9 and  $412\text{ nm}$  for  $\text{CH}_2\text{O}$  (after resting for 1 h in the dark). From the UV–vis absorption curves, kinetic constants for the  $\text{TiO}_2$  photocatalyzed AB9 degradation were obtained by assuming a first-order reaction (eq 3):

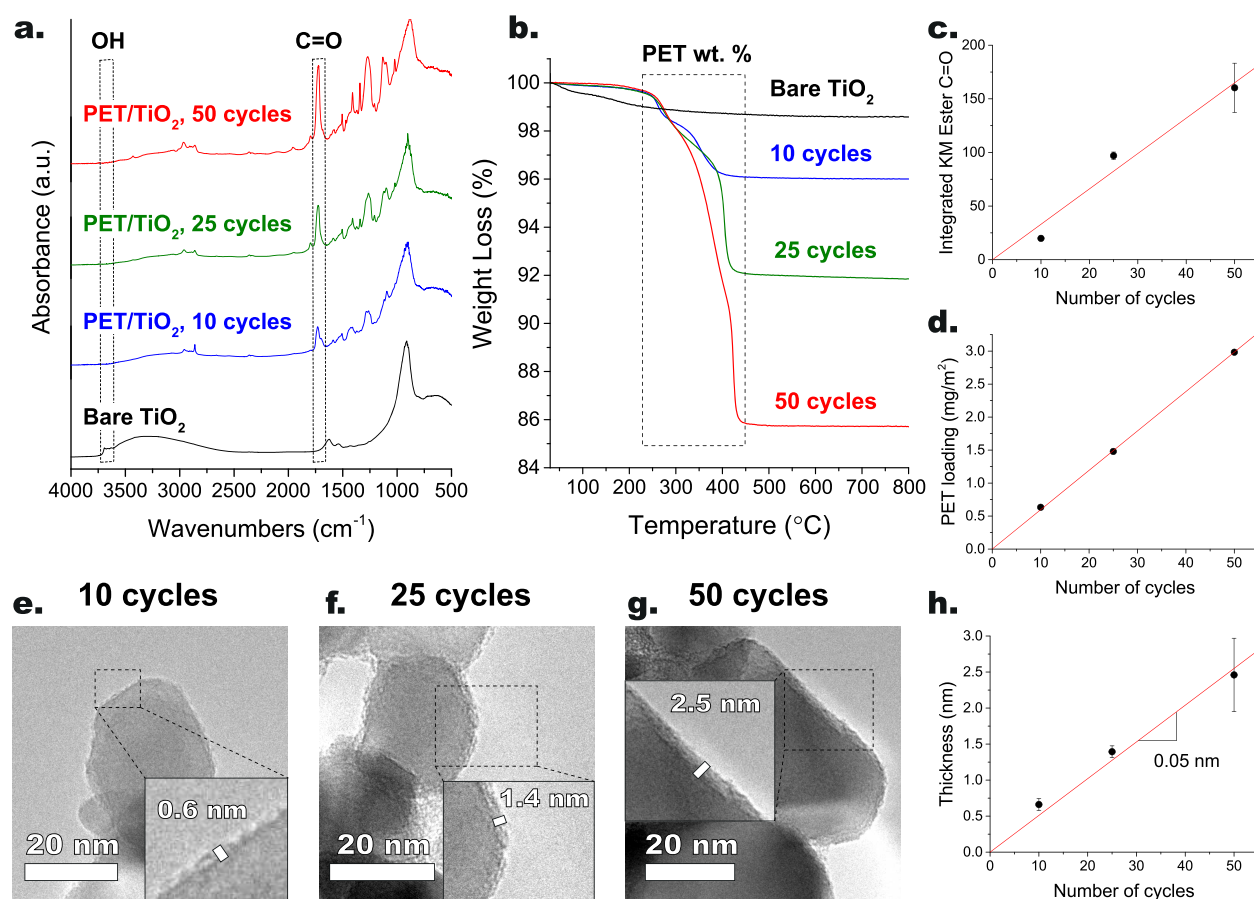


**Figure 2.** Linear PET film growth as a function of the MLD cycles. (a, c) Evolution of characteristic PET features with cycle number. (a) DRIFTS spectra of bare and PET-coated TiO<sub>2</sub>. (c) Evolution of ester carbonyl (C=O) stretch, centered around 1725 cm<sup>-1</sup>, evaluated by its area in the Kubelka–Munk spectra. (b, d) Evolution of PET loading with cycle number. (b) TGA thermograms of bare and PET-coated TiO<sub>2</sub>. (d) Evolution of PET deposited amount, evaluated by the weight loss between 225 and 450 °C, and then expressed in mg/m<sup>2</sup>. (e–h) Evolution of PET film thickness with cycle number. TEM images of PET-coated TiO<sub>2</sub> nanoparticles after (e) 10 cycles, (f) 25 cycles, and (g) 50 cycles. (h) Evolution of PET film thickness, measured by ImageJ.

$$C_{AB9} = C_{AB9,0} \exp(-k_{app,AB9}t) \quad (3)$$

where  $C_{AB9,0}$  and  $C_{AB9}$  are the initial concentration and the concentration at the time  $t$  of AB9, respectively, and  $k_{app,AB9}$  is the apparent first-order kinetic constant that represents the reaction rate. Methanol oxidation to formaldehyde can instead be treated as a zero-order reaction<sup>43</sup> (eq 4):

$$C_{CH_2O} = k_{app,CH_2O}t \quad (4)$$

where  $C_{CH_2O}$  is the concentration of CH<sub>2</sub>O at the time  $t$  and  $k_{app,CH_2O}$  is the apparent zero-order kinetic constant.

UV–vis diffuse reflectance spectroscopy measurements were performed using a PerkinElmer-Lambda 900 spectrometer equipped with an integrated sphere device. The spectra were acquired in the wavelength range 700–250 nm, with fine steps of 1 nm.

The specific surface area (SSA) of the nanoparticles was measured by a Brunauer–Emmett–Teller (BET) N<sub>2</sub>-sorption surface area analyzer (Micromeritics TriStar 3020). Around 100 mg of nanopowders was used for each measurement. Prior to the measurement, the nanopowders were degassed for at least 2 days at 25 °C under vacuum using VacPrep (Micromeritics).

Electron paramagnetic resonance measurements were carried out using a Bruker EMXplus spectrometer equipped with an ER4102ST resonator (Bruker) with optical access provided by a grid with 50% transmittance. The generation of hydroxyl radical species ( $g = 2.0067$ ,  $A_N = 15.0$  G,  $A_H = 14.7$  G) was evaluated with the radical adduct 5,5-dimethyl-1-pyrroline *N*-oxide (DMPO), used as a spin-trap agent.

Suspensions with a volume of 10 μL containing 50 mM DMPO and 1 mg/mL TiO<sub>2</sub> (the same concentration used in the photocatalytic tests) were prepared in an EPR quartz sample tube (inner diameter of 1 mm) and placed into the spectrometer. The samples were then irradiated with a 365 nm UV laser light (uvBeast UV Flashlight MINI) for the photocatalytic generation of radical species. EPR spectra without and with UV illumination were recorded from 343.8 to 353.8 mT. The following parameters were used: microwave frequency, 9.793 GHz; microwave power, 20 mW; modulation frequency, 100 kHz; modulation amplitude, 0.1 mT; room temperature. The experimental spectra were finally simulated using the SpinFit software (Bruker).

Zeta potential measurements of 1 mg/mL nanoparticle suspensions (on the basis of uncoated TiO<sub>2</sub> P25 mass) were taken with a Zetasizer Nano ZS (Malvern Instruments) and built-in software. Samples were calibrated for 5 min, and values were averaged over 10 measurements, with 40 runs per measurement.

## RESULTS AND DISCUSSION

**Deposition of Sub-nanoscale and Nanoscale PET Films.** The defining characteristic of MLD is the self-limiting, layer-by-layer growth of the organic film. We assessed whether PET can be grown in a self-saturating manner on gram-scale batches of TiO<sub>2</sub> P25 NPs with ex-situ DRIFTS and TGA. Specifically, we tracked the ester carbonyl stretch in the DRIFTS spectra, and the weight loss corresponding to the amount of deposited organic matter in the TGA thermograms,

as a function of the precursor exposure times (see Figures S1 and S2). The integrated Kubelka–Munk ester carbonyl (O=C=O) stretch and deposited organic matter follow comparable evolutions. In particular, the DRIFTS spectra show that, with increasing TC exposures, the O=C=O peak sharply increases until  $\sim 1$  min of TC, after which it remains relatively constant (see Figures S1b and S2). Moreover, the spectrum for a 3 min exposure time of TC reveals the emergence of the chlorinated carbonyl stretch (Cl-C=O), arising from TC. This translates into an additional deposition of organic matter, as evidenced by TGA, thus suggesting that after 1 min of TC pulsing the growth predominantly proceeds via the adsorption of unreacted precursor, rather than the deposition of PET (see Figures S1a and S3). In fact, bifunctional organic precursors such as TC are typically very sticky molecules that are difficult to purge.<sup>44</sup> This nonideal behavior is also reported for other diacyl chloride and diisocyanate precursors.<sup>45,46</sup> In contrast, ideal self-limiting behavior is observed for increasing EG exposures with a saturation time of  $\sim 1$  min (see Figure S1c,d).

On this basis, we then demonstrated the linear evolution of the PET MLD growth using exposure times of 1 min for both precursors in separate experiments of 10, 25, and 50 cycles (see Figure 2). The ester carbonyl stretching vibration, deposited organic matter, and film thickness all linearly increase with the number of cycles (see Figure 2c,d,h). In particular, the agreement between FTIR and TGA analyses indicates that the deposited organic material is the desired PET film. Figure 2a displays the DRIFTS absorbance spectra of bare TiO<sub>2</sub>, fluidized at 150 °C to mimic the MLD reaction conditions, and PET-coated TiO<sub>2</sub> after 10, 25, and 50 cycles. The peaks in the 3700–3600 cm<sup>-1</sup> region of the bare TiO<sub>2</sub> spectra, attributed to OH surface groups,<sup>47</sup> disappear upon PET deposition. The hydroxyl groups on the TiO<sub>2</sub> surface react, in fact, with TC, thus confirming the chemisorption of the PET film. Moreover, the broad shoulder from 3600 to 2500 cm<sup>-1</sup>, arising from the presence of adsorbed H<sub>2</sub>O molecules, as well as the peak at 1625 cm<sup>-1</sup>, corresponding to  $\delta(\text{H}_2\text{O})$ , vanishes.<sup>48</sup> The strong absorption band at around 1725 cm<sup>-1</sup> is characteristic of the ester C=O group. Typically, the saturated aliphatic ester is in the 1750–1735 cm<sup>-1</sup> region. However, the conjugation of the C=O group with an aryl group lowers the absorption frequency.<sup>49</sup> Other peaks characteristic of PET are the CH<sub>2</sub> stretches at 2970 and 2908 cm<sup>-1</sup>, the C(=O)–O stretches at 1130 and 1270 cm<sup>-1</sup>, the symmetric C–O stretch at 1100 cm<sup>-1</sup>, and the antisymmetric C–O stretches at 1042 and 971 cm<sup>-1</sup> (see Figure 2 and Figure S4).<sup>50–52</sup> Moreover, the benzene ring exhibits in-plane vibrations at 1960, 1615, 1585, 1506, 1410, and 1022 cm<sup>-1</sup>.<sup>53</sup> Interestingly, the peak increase in the trans rotational conformers of the EG moiety (i.e., CH<sub>2</sub> bending at 1471 cm<sup>-1</sup>, CH<sub>2</sub> wagging at 1342 cm<sup>-1</sup> and antisymmetric C–O stretching at 971 cm<sup>-1</sup>) relative to the gauche conformers (i.e., CH<sub>2</sub> bending at 1456 cm<sup>-1</sup>, CH<sub>2</sub> wagging at 1371 cm<sup>-1</sup> and antisymmetric C–O stretching at 1042 cm<sup>-1</sup>) as well as the appearance of the in-plane C–H bending mode of the benzene ring at 1388 cm<sup>-1</sup> and the reduction in the in-plane C–H bending at 1174 cm<sup>-1</sup> suggest an increasing degree of crystallinity with the number of cycles.<sup>53</sup> The growth of the ethylene terephthalate oligomer with increasing cycles likely involves an increasing physical interconnectivity between chains and, thus, may increase ordering of the molecular chains.

The weak absorbance peak at 1795 cm<sup>-1</sup>, which is attributed to the Cl–C=O stretch, may be a result of steric effects hindering the access of EG to the chemisorbed TC, or may be caused by physisorbed TC within the growing film. We investigated the possibility to remove this TC impurity by performing a series of thermal annealing trials at different temperatures in an inert gas (N<sub>2</sub>) within a TGA furnace. DRIFTS spectra indicate that annealing at 200 °C for 3 h is sufficient to remove nearly all the chlorine signal, without affecting any other absorbance peak (see Figure S5). This suggests that the Cl–C=O peak is due to physisorbed TC, which is difficult to remove at the reaction temperature and with the purging times used in the MLD process. As PET possesses good thermal stability, with a melting point around 260 °C,<sup>54</sup> this is a promising approach to obtain higher quality films. Furthermore, this treatment can be directly carried out in the fluidized-bed MLD reactor, allowing a two-step batch process within the same unit.

The amount of deposited PET was measured by analyzing the TGA thermograms. Bare TiO<sub>2</sub> P25 shows a weight loss up to 120 °C of  $\sim 0.87\%$  due to physically adsorbed water and from 120 to 500 °C of an additional  $\sim 0.87\%$  due to chemically bound water.<sup>55</sup> Instead, PET-coated TiO<sub>2</sub> does not exhibit any weight loss from physisorbed or chemisorbed water due to its hydrophobic nature, as we will discuss later. The PET loading, expressed as wt %, corresponds to the weight loss of PET-coated TiO<sub>2</sub> in the temperature range between 225 and 450 °C (see Figure 2b). This demonstrates that the PET sub-nanofilm and nanofilms are thermally stable up to  $\sim 225$  °C. When plotted as a function of the number of cycles, the PET loading, expressed as mg/m<sup>2</sup> (eq 1), displays a linear evolution (see Figure 2d).

Analogously, TEM observations provided further evidence of the linear increase in PET film growth. The average PET thickness was 0.6, 1.4, and 2.5 nm after 10, 25, and 50 cycles, respectively (see Figure 2e–g). To understand whether the film thicknesses observed under TEM were also consistent with the loadings measured by TGA, we calculated the thickness of the PET film resulting from the PET loading, according to eq 2. The calculated thicknesses were almost identical to the thicknesses observed under TEM (see Figure S6). The small deviation can be attributed to an overestimation of PET density, which is likely to be lower than 1.38 g/cm<sup>3</sup>, as the MLD-grown low-molecular-weight PET nanofilms are expected to be less dense than bulk PET. These film thicknesses translate into a growth per cycle (GPC) of  $\sim 0.05$  nm (see Figure 2h). This GPC is significantly lower than the extended vertical length of the ethylene terephthalate monomer, which is 1.1 nm.<sup>56</sup> This phenomenon is widely reported in several MLD processes and is generally attributed to the tilted orientation of the polymer chains and double reaction terminations which can occur when using bifunctional organic precursors.<sup>44,49,57</sup> Bergsman et al.<sup>57</sup> demonstrated the tilted orientation of MLD-grown polyurea films, which present an average chain angle of 25°, as well as the dependence of double reaction terminations on monomer flexibility. In particular, the more flexible the monomer is, the higher the probability of chain terminations is, and thus the lower the GPC is. Furthermore, their analyses suggest that MLD films consist of a mixture of upwardly growing chains and horizontally aligned polymer segments. Similarly, Peng et al.<sup>58</sup> found that polyamide films grown from TC and 1,4-diaminobutane lie nearly parallel to the surface. Therefore, the

low GPC of PET MLD likely arises mainly from polymer chains growing parallel to the surface instead of perpendicularly, as well as from double reaction terminations that reduce the surface site density. Still, the linear growth of the MLD film is retained thanks to the equilibrium between double reaction terminations and monomer renucleation, which introduces new reaction sites for the growth to recover.<sup>59</sup>

To further demonstrate that the low GPC of PET MLD was not limited to fluidized TiO<sub>2</sub> NPs, we also deposited PET on flat Si wafers. The wafers were first treated in a UV ozone cleaner to produce a native SiO<sub>2</sub> surface layer and then coated for 75 TC/EG cycles in an atmospheric-pressure ALD chamber. The film thicknesses measured at different growth cycles by spectroscopic ellipsometry result in a GPC of  $\sim 0.07$  nm, comparable to that found for fluidized TiO<sub>2</sub> NPs (Figure S7). Furthermore, these GPCs are in agreement with the  $\sim 0.05$  nm GPC reported by Ivanova et al.<sup>49</sup> on OH-terminated Si wafers in a commercial vacuum ALD reactor. This indicates that the very low GPC of PET MLD is inherent to the surface chemistry involved as well as to the reaction temperature used. In fact, at the relatively high temperature of 150 °C used here, thermally driven desorption of precursors can take place,<sup>60</sup> thereby contributing to the decrease of the GPC.

Finally, we investigated the chemical state of the TiO<sub>2</sub> NPs by XPS (see Figure 3). The Ti 2p spectra of both bare and PET-coated TiO<sub>2</sub> show that the Ti atoms are mostly in the Ti<sup>4+</sup> state, with a small fraction in the Ti<sup>3+</sup>, indicating that the MLD process does not affect the chemical state of Ti (see Figure 3b and Figure S8b). The deconvolution of the O 1s and C 1s spectra reveals an increase in the peaks attributed to the O–C=O group with the number of MLD cycles, further confirming the deposition of PET on both TiO<sub>2</sub> NPs and Si wafers (Figure 3a, Figures S8a and S9).<sup>61</sup> Both bare TiO<sub>2</sub> NPs and Si wafers contain carbon species likely arising from adventitious carbon and/or from the carbon tape used in the XPS sample preparation.<sup>10</sup> Furthermore, the peak associated with the Ti–O bond in the O 1s spectra shifts toward higher binding energies with increasing cycles due to the difference in electronegativities among Ti (1.54), O (3.44), H (2.2), and C (2.55). As the electronegativity of C is higher than those of Ti and H, the electron density around O decreases, and thus, the binding energy increases. This demonstrates the formation of Ti–O–C linkages at the interface between TiO<sub>2</sub> and PET.

**Effect of PET Deposition on TiO<sub>2</sub> Photoactivity.** The suppressive effect of the sub-nanoscale and nanoscale PET films on the photocatalytic properties of TiO<sub>2</sub> P25 was quantified by the photodegradation of the Acid Blue 9 (AB9) dye and by the oxidation of methanol (MeOH) to formaldehyde (CH<sub>2</sub>O). In particular, MeOH oxidation was performed to test the ability of the PET films to suppress TiO<sub>2</sub> photoactivity against small organic molecules. Aliquots of the TiO<sub>2</sub> suspensions were taken at various time intervals, and the corresponding concentrations were evaluated as a function of AB9 and CH<sub>2</sub>O absorption peaks at 629 and 412 nm, respectively. Photocatalyzed dye degradation is treated as a first-order reaction (see eq 3), and therefore, the kinetic constant can be obtained from the slope of the linear fit of the logarithm of the dye concentration as a function of UV irradiation time. The AB9-only solution control shows no change in dye concentration with irradiation time, whereas the AB9-bare TiO<sub>2</sub> suspension displays a clear decrease, indicative of the high dye degradation rate photocatalyzed by TiO<sub>2</sub> NPs (see Figure 4a). Analogously, the blank MeOH-only solution

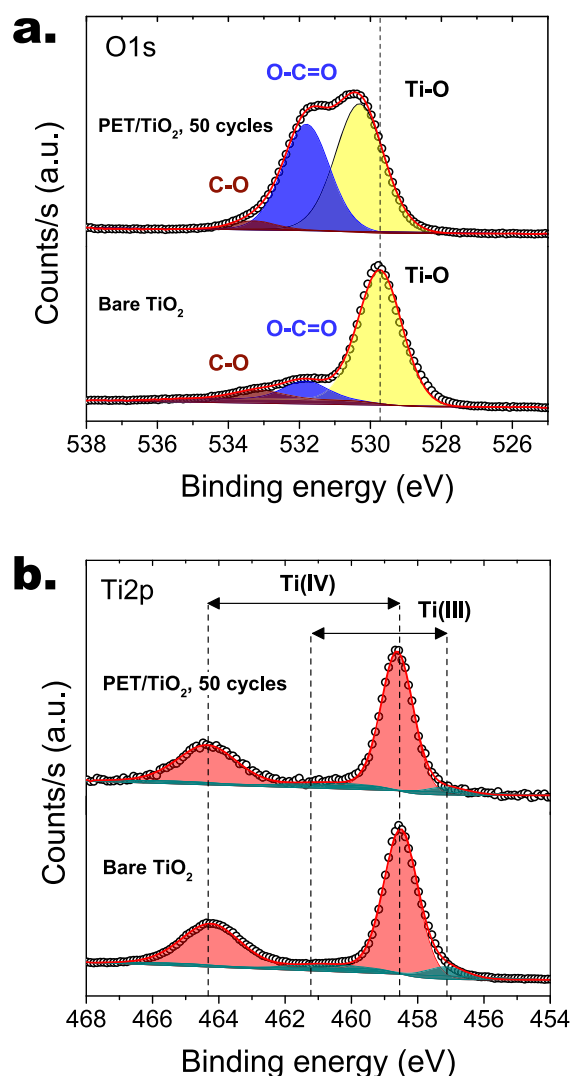


**Figure 3.** (a) O 1s and (b) Ti 2p XPS spectra of bare and PET-coated TiO<sub>2</sub> for 50 cycles.

does not exhibit any formation of CH<sub>2</sub>O, while the MeOH-bare TiO<sub>2</sub> suspension results in a significant increase in CH<sub>2</sub>O concentration, denoting the ability of TiO<sub>2</sub> to photocatalyze the methanol oxidation (see Figure 4b). MeOH oxidation is a zero-order reaction (see eq 4) considering the excess of MeOH present in solution, and thus, the kinetic constant corresponds to the slope of the linear fit of the CH<sub>2</sub>O concentration as a function of the irradiation time. Compared to bare TiO<sub>2</sub>, PET-coated TiO<sub>2</sub> photodegrade AB9 and photo-oxidizes MeOH at a significantly reduced rate. Specifically, an exponential decay in the kinetic constant is found with increasing cycle number, from a 7.5-fold drop after 10 cycles to a  $\sim 14$ -fold drop after 50 cycles for AB9 degradation, and from a  $\sim 5$ -fold drop after 10 cycles to a  $\sim 9$ -fold drop after 50 cycles for MeOH oxidation (see Figure 4c). Given that the photocatalytic oxidation of MeOH proceeds through the holes trapped on the TiO<sub>2</sub> surface,<sup>62</sup> this demonstrates that even sub-nanoscale PET films of  $\sim 0.6$  nm can prevent molecules as small as MeOH from reaching the TiO<sub>2</sub> surface and, thus, substantially suppress the photoactivity of TiO<sub>2</sub>. Therefore, the PET films are suitable candidates to prevent the TiO<sub>2</sub>-induced photo-

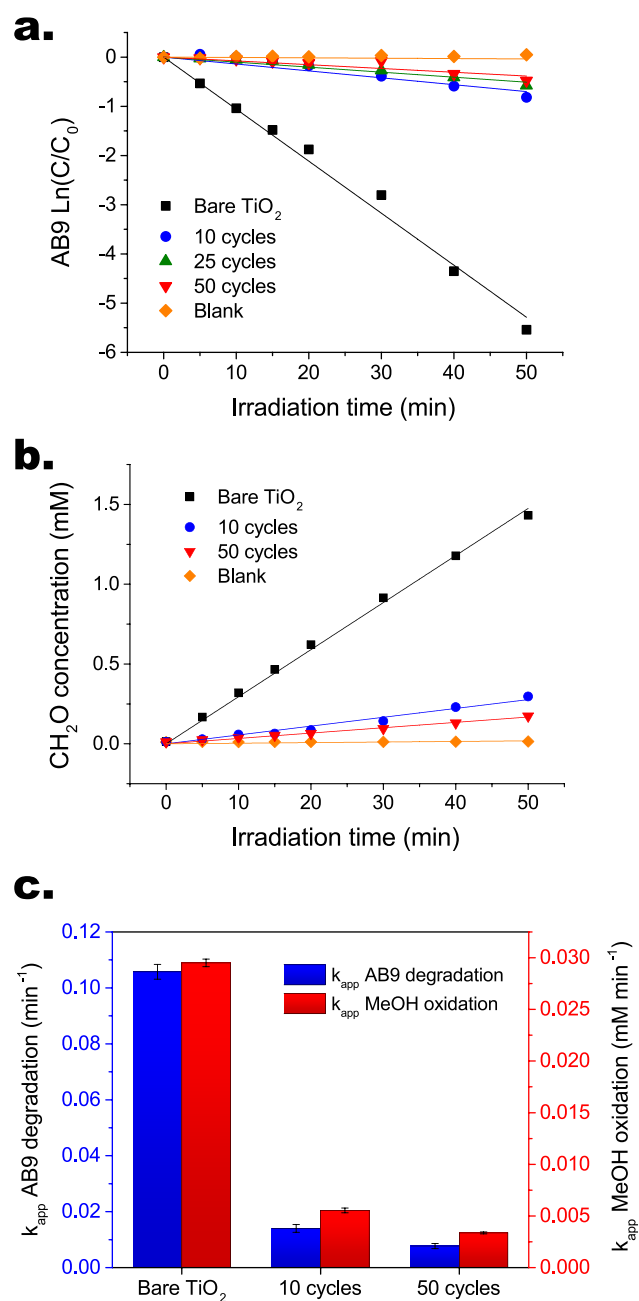


**Figure 4.** Photocatalytic test of Acid Blue 9 (AB9) degradation and methanol oxidation with bare and PET-coated  $\text{TiO}_2$ . (a) Evolution of the natural log of AB9 concentration as a function of irradiation time. The reaction is of the first order:  $\ln(C/C_0) = -k_{\text{app}}t$ . (b) Evolution of the formaldehyde concentration as a function of irradiation time. The reaction is zero-order:  $C = k_{\text{app}}t$ . (c) Decrease in apparent kinetic constant with cycle number, obtained from the slope of the linear fittings in panels a and b.

degradation of large organic molecules, such as polymers, dyes, and colorants, present in paints and cosmetics.

A number of factors could explain the observed reduction in the photocatalytic activity of the  $\text{TiO}_2$  P25 NPs. Significantly altering the material properties of the  $\text{TiO}_2$  NPs, such as their UV–vis absorption, or the NP electronic structure, or drastically decreasing the surface area available for illumination could suppress the rate of AB9 degradation and MeOH oxidation. UV–vis diffuse reflectance spectroscopy (UV-DRS)

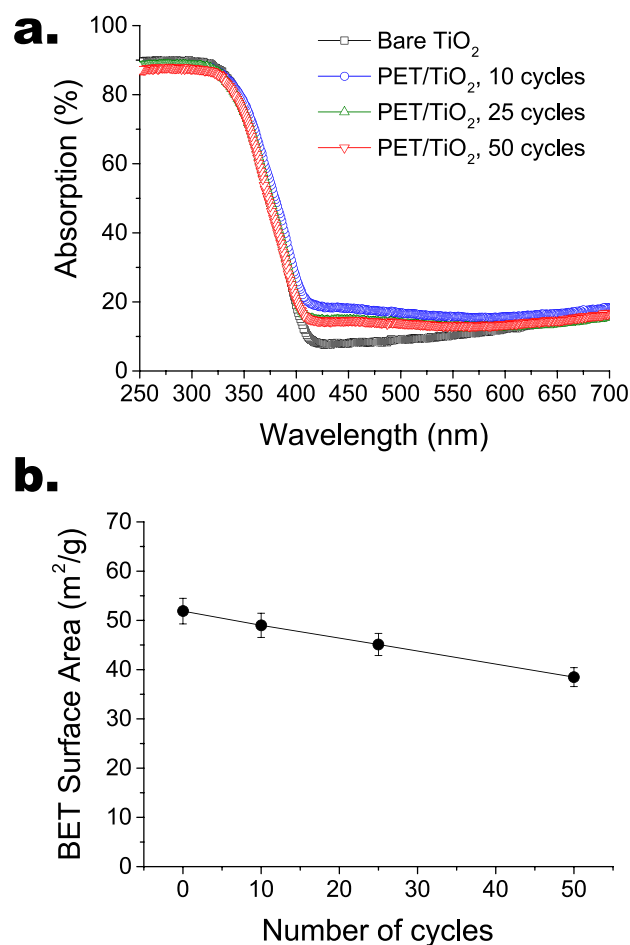


**Figure 5.** (a) UV–vis absorption spectra of bare and PET-coated  $\text{TiO}_2$ . The slight increase in the light absorption from 400 to 600 nm after MLD is attributed to the PET film. (b) BET surface area of bare and PET-coated  $\text{TiO}_2$  for 10, 25, and 50 cycles. The slight decrease in surface area can be attributed to minor agglomeration phenomena occurring during the MLD process.

shows that the absorption properties of  $\text{TiO}_2$  are relatively unaffected by the MLD process (see Figure 5a). Only a slightly higher visible light absorption is observed in the 400–600 nm range due to the presence of PET. The retention of the powder optical properties, e.g., whiteness (see also Figure S10), despite the coating with organic films, is not generally achievable via conventional liquid-phase approaches,<sup>63</sup> thus indicating the greater applicability of MLD. XPS analysis previously indicated that the electronic structure of Ti is unchanged by the MLD process (see Figure 3b). BET measurements display a slight decrease in the specific surface area (SSA) with the number of cycles (see Figure 5b). However, as shown in Table S1, higher values for the SSA of PET-coated  $\text{TiO}_2$  are expected with an increasing number of cycles, due to the proportionally larger decrease in particle density compared to the increase in particle diameter. The slight reduction in SSA can be attributed to minor agglomeration phenomena occurring during the MLD process, likely induced by the sticky nature of the organic precursors which might promote particle agglomeration. Therefore, the UV–vis absorption and electronic properties as well as the surface area of the PET-coated NPs cannot explain the drastic reduction in the photoactivity of  $\text{TiO}_2$ .

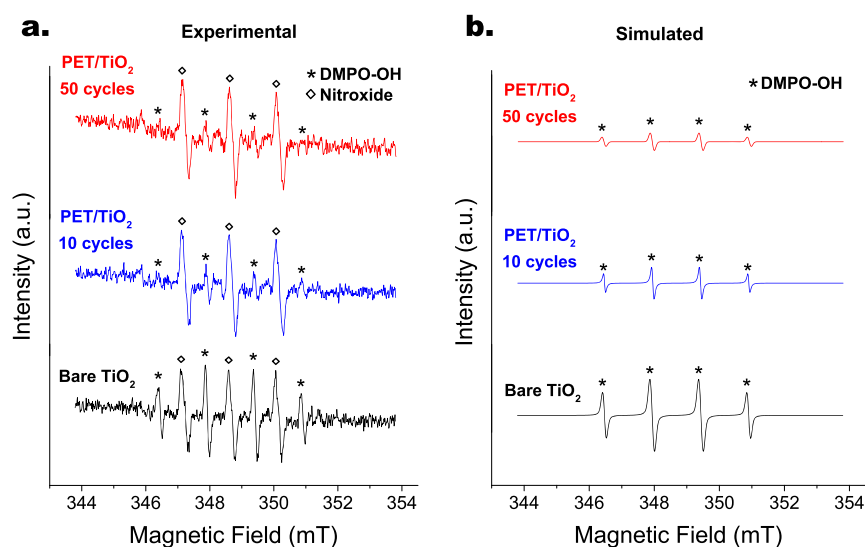


**Figure 6.** EPR spectra of OH radical adduct species trapped by DMPO in bare and PET-coated TiO<sub>2</sub> aqueous dispersions under UV irradiation. (a) Experimental spectra. The asterisks indicate the OH radical DMPO adduct species generated by TiO<sub>2</sub>. The background peaks at 347.1, 348.6, and 350.1 mT, marked by the diamonds, are attributed to nitroxide-radical species arising from contaminations or degradation of the DMPO used. (b) Simulated spectra. The simulated background nitroxide-radical peaks are removed to highlight the change in the DMPO–OH adduct signal.

To further investigate the origin of the observed photocatalytic suppression, electron paramagnetic resonance (EPR) measurements were performed under UV illumination to probe the formation of hydroxyl radicals in solution. The hydroxyl radical was analyzed due to its status as the primary oxidant in aqueous photocatalytic systems.<sup>64</sup> EPR spectra of the suspensions containing bare or PET-coated TiO<sub>2</sub> NPs and the spin-trap DMPO were taken during UV irradiation and then simulated using the SpinFit software. The spin trap reacts with free radicals at or near the TiO<sub>2</sub> surface to generate more stable products referred to as spin adducts, which can be observed by EPR. In particular, DMPO is highly beneficial when identifying hydroxyl radicals as it forms the DMPO–OH adduct, which is characterized by a 4-peak symmetric spectrum with the relative intensity ratio of 1:2:2:1. The PET-coated TiO<sub>2</sub> samples show a clear reduction in the intensity of the DMPO–OH adduct peaks, indicating that the PET films significantly suppress the generation of hydroxyl radical species (see Figure 6). The 3 background peaks at 347.1, 348.6, and 350.1 mT are attributed to nitroxide-radical species arising from contaminations or degradation of the stock DMPO solution and are present with a similar amplitude even prior to UV irradiation (see Figure S11). The observed reduction in hydroxyl radicals is mainly attributed to the ability of the PET films to block the adsorption of water and reactant molecules onto the TiO<sub>2</sub> surface. It is worth noting that the PET MLD process eliminates the OH groups on the TiO<sub>2</sub> surface, as shown in the DRIFTS spectra in Figure 2a, which are known to play a crucial role in the TiO<sub>2</sub> photocatalytic activity.<sup>65</sup> However, the TiO<sub>2</sub> surface dehydroxylation alone cannot explain the observed photocatalytic suppression. The main role is, in fact, played by the PET film barriers which are capable of providing photosuppression against a broad range of molecule sizes, from the small MeOH molecules to the large AB9 molecules. MeOH is oxidized by the photogenerated holes trapped on the TiO<sub>2</sub> surface, thus necessitating an intermediate adsorption step onto TiO<sub>2</sub>.<sup>62</sup> Dye degradation typically follows a Langmuir–Hinshelwood mechanism, which also requires the adsorption of the dye onto the TiO<sub>2</sub> surface.<sup>66</sup> Finally, DMPO

mainly reacts with photogenerated holes and/or hydroxyl radicals at or near the surface rather than in the bulk solution.<sup>67,68</sup> Therefore, the MLD-grown PET films prevent the access of water and reactant molecules to the TiO<sub>2</sub> surface, thus preventing the migration of photogenerated charge carriers from TiO<sub>2</sub> surface to the reactants, and reducing the formation of hydroxyl radicals. Most interestingly, the sub-nanofilms obtained after 10 cycles are sufficient to suppress the photocatalytic activity, highlighting the potential of MLD for surface modification on length-scales not typically attainable with alternative approaches. In particular, suppressing the formation of reactive oxygen species is of interest due to their negative biological effects,<sup>6</sup> suggesting potential applications for surface passivation in fields such as nanomedicine.

**Effect of PET Deposition on TiO<sub>2</sub> Dispersibility.** We then investigated the dispersibility of the TiO<sub>2</sub> NPs in both aqueous and organic media. After dispersion of the nanopowders in water, it was macroscopically observed that PET-coated TiO<sub>2</sub> produced more stable suspensions than bare TiO<sub>2</sub> (see Figure 7a). In fact, while the bare TiO<sub>2</sub> NPs fully sedimented within 3 h, the PET-coated TiO<sub>2</sub> NPs remained dispersed for several hours. To obtain a more quantitative estimation of the dispersion stability, zeta potential measurements of NP suspensions were taken. With increasing cycle number, the zeta potential of the NPs in demineralized water drops from –2.8 mV for bare TiO<sub>2</sub> to –26.8 mV for PET-coated TiO<sub>2</sub> after 50 cycles (see Figure 7b). No meaningful variance in pH was found across the different suspensions, indicating that the decrease in zeta potential is indeed a result of the PET films. In fact, across the pH range measured, PET surfaces possess a more negative zeta potential than TiO<sub>2</sub> P25.<sup>69–71</sup> The determined zeta potentials are therefore in good agreement with the observed greater stability of aqueous PET-coated TiO<sub>2</sub> dispersions. The sub-nanoscale and nanoscale PET films stabilize the TiO<sub>2</sub> NPs by electrostatic repulsion, thus preventing them from aggregating. Moreover, it is worth stressing that the MLD-grown PET films are stable in water, as opposed to hybrid ALD/MLD films such as alucone.<sup>72</sup>

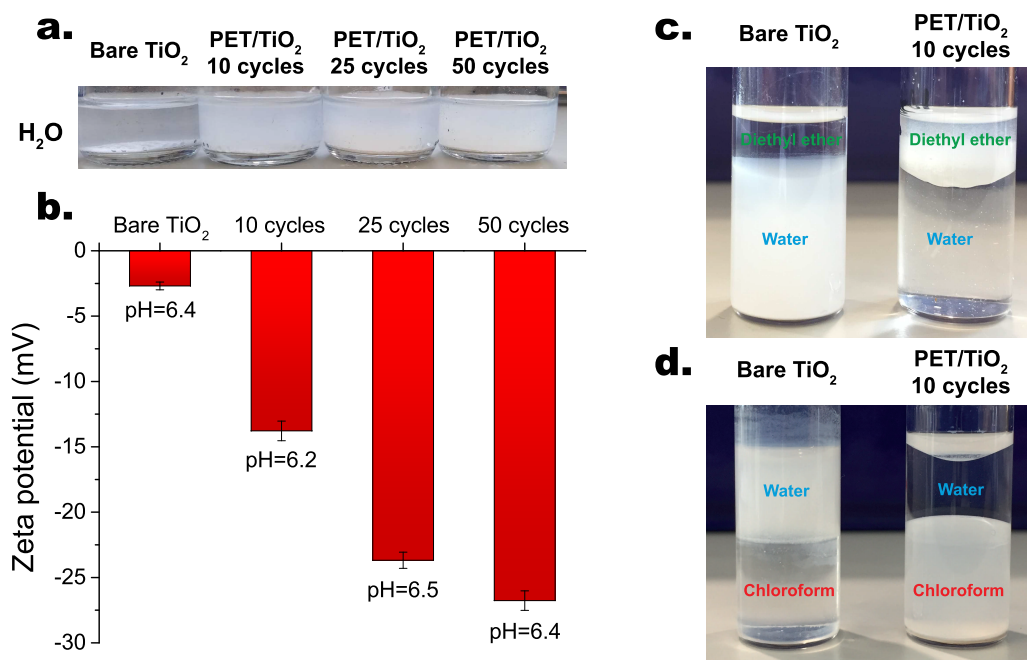


**Figure 7.** Dispersibility of bare and PET-coated TiO<sub>2</sub> in water and organics. (a, b) Stability of bare and PET-coated TiO<sub>2</sub> dispersions in water. (a) Pictures of bare and PET-coated TiO<sub>2</sub> dispersions in water after resting for 1 h. (b) Decrease in zeta potential with the number of MLD cycles, indicating increasing dispersion stability. (c, d) Dispersion of bare and PET-coated TiO<sub>2</sub> in (c) diethyl ether/water mixture and (d) chloroform/water mixture.

More importantly, organic coatings can improve the dispersibility of particles in organic media.<sup>73</sup> Mixtures of an apolar organic solvent, namely, diethyl ether (Et<sub>2</sub>O) or chloroform (CHCl<sub>3</sub>), and water were prepared. Diethyl ether and chloroform were selected for their relative immiscibility with water and different specific gravities. Et<sub>2</sub>O has a lower density than H<sub>2</sub>O and, thus, is the upper phase, whereas CHCl<sub>3</sub> is more dense than H<sub>2</sub>O, and thus constitutes the lower phase. Both bare and 10-cycle-PET-coated TiO<sub>2</sub> powders were placed in the organic–water mixtures and vigorously shaken. A clear change in the dispersion properties of TiO<sub>2</sub> was observed as a result of the PET deposition (see Figure 7c,d). The hydroxyl surface species on bare TiO<sub>2</sub> gives it a highly hydrophilic character, which favors the water phase. On the other hand, PET-coated TiO<sub>2</sub> preferentially disperses within the organic phase, indicating the hydrophobization of the NPs following the MLD process. Modifying the phase in which the PET-coated powders were first dispersed did not affect the final phase separation. Therefore, the sub-nanofilms are able to completely alter the dispersion properties of the NPs. This enhancement of particle dispersibility in organic media is of great interest for various applications, such as the production of organic-based paints, nanofluids, Pickering emulsions, and polymer nanocomposites.

Furthermore, the PET films offer advantages in terms of chemical stability over other organic coatings. As a demonstration, dispersions of poly(ethylene malonate)-MLD-coated TiO<sub>2</sub> in Et<sub>2</sub>O/H<sub>2</sub>O mixtures were tested. Polyethylene malonate (PEM) was chosen as an aliphatic polyester reference which can be obtained by MLD. The PEM film did not affect the hydrophilicity of TiO<sub>2</sub> NPs for a noticeable period of time, as, immediately after mixing, a large portion of PEM-coated TiO<sub>2</sub> NPs are found in the water phase (see Figure S12). This is attributed to the poor chemical resistance of PEM to the Et<sub>2</sub>O solvent. In contrast, PET demonstrates a good chemical

resistance to an extensive range of organic solvents, thus expanding its applicability. Finally, the ultrathin PET films show good resistance to UV-light irradiation. DRIFTS and TGA analysis as well as Et<sub>2</sub>O/H<sub>2</sub>O dispersion tests confirm that the PET films are unaltered after exposure to UV light for 1 h (see Figure S13), which is the approximate duration of the photocatalytic test. Therefore, PET constitutes a promising organic material for ultrathin films due to its good thermal, chemical, and UV-light stability.

## CONCLUSION

In conclusion, we have demonstrated the deposition of sub-nanoscale and nanoscale PET films on TiO<sub>2</sub> P25 nanopowders by MLD. Ex-situ DRIFTS, TGA, and TEM confirm the presence of PET and its linear growth with the number of cycles. The low GPC of 0.05 nm on fluidized TiO<sub>2</sub> is in agreement with that obtained on Si wafers in both vacuum and atmospheric-pressure reactors. The PET films are able to suppress the photoactivity of TiO<sub>2</sub> NPs by reducing the access of water and reactant molecules to the TiO<sub>2</sub> surface, and thus the generation of hydroxyl radicals involved in the photocatalytic reactions. At the same time, the bulk optical properties, e.g., whiteness, of TiO<sub>2</sub> are retained, which is not typically possible with traditional liquid-phase organic coating methods. Furthermore, the PET films deliver greater stability to the TiO<sub>2</sub> NP suspensions in water and enhance the dispersibility of TiO<sub>2</sub> NPs in organic solvents. Such properties are of relevance to the paints and cosmetics industries, where TiO<sub>2</sub> NPs are widespread, and it is crucial to prevent the degradation of large organic compounds such as polymers, dyes, and colorants. For these reasons, the ability of MLD to produce sub-nanoscale organic films on large quantities of nanopowders in scalable atmospheric-pressure fluidized-bed reactors is of commercial interest. Finally, modifying the dispersion properties of particles in a swift and controllable

manner by surface engineering at the sub-nanometer level can open up new research directions for future MLD studies.

## ■ ASSOCIATED CONTENT

### SI Supporting Information

The Supporting Information is available free of charge at <https://pubs.acs.org/doi/10.1021/acsnm.0c01158>.

Saturation curves, DRIFTS spectra of PET-coated TiO<sub>2</sub> with different TC times, TEM image of PET-coated TiO<sub>2</sub> for long precursor times, FTIR peak assignment, DRIFTS spectra of annealed PET-coated TiO<sub>2</sub>, PET thickness calculated from TGA analysis, ellipsometry of PET films on Si wafer, XPS of bare and PET-coated TiO<sub>2</sub> and Si wafer, photos of bare and PET-coated TiO<sub>2</sub> powders, EPR spectra under visible light irradiation, dispersion of PEM-coated TiO<sub>2</sub> in Et<sub>2</sub>O/H<sub>2</sub>O mixture, and stability of PET-coated TiO<sub>2</sub> to UV-light irradiation (PDF)

## ■ AUTHOR INFORMATION

### Corresponding Author

**Damiano La Zara** – Department of Chemical Engineering, Delft University of Technology, 2629HZ Delft, The Netherlands; [orcid.org/0000-0002-0967-7451](https://orcid.org/0000-0002-0967-7451); Email: [d.lazara@tudelft.nl](mailto:d.lazara@tudelft.nl)

### Authors

**Maximilian R. Bailey** – Department of Chemical Engineering, Delft University of Technology, 2629HZ Delft, The Netherlands; Laboratory for Soft Materials and Interfaces, Department of Materials, ETH Zurich, 8093 Zurich, Switzerland; [orcid.org/0000-0003-0350-598X](https://orcid.org/0000-0003-0350-598X)

**Peter-Leon Hagedoorn** – Department of Biotechnology, Delft University of Technology, 2629HZ Delft, The Netherlands

**Dominik Benz** – Department of Chemical Engineering, Delft University of Technology, 2629HZ Delft, The Netherlands; [orcid.org/0000-0001-9025-0174](https://orcid.org/0000-0001-9025-0174)

**Michael J. Quayle** – AstraZeneca R&D Gothenburg, Mölndal SE-431 83, Sweden; [orcid.org/0000-0001-5782-6506](https://orcid.org/0000-0001-5782-6506)

**Staffan Folestad** – AstraZeneca R&D Gothenburg, Mölndal SE-431 83, Sweden; [orcid.org/0000-0001-8069-6156](https://orcid.org/0000-0001-8069-6156)

**J. Ruud van Ommen** – Department of Chemical Engineering, Delft University of Technology, 2629HZ Delft, The Netherlands; [orcid.org/0000-0001-7884-0323](https://orcid.org/0000-0001-7884-0323)

Complete contact information is available at: <https://pubs.acs.org/doi/10.1021/acsnm.0c01158>

### Author Contributions

<sup>†</sup>D.L.Z. and M.R.B. contributed equally to this work.

### Notes

The authors declare the following competing financial interest(s): J.R. van Ommen has a financial interest in Delft IMP.

## ■ ACKNOWLEDGMENTS

The authors thank Lois van Druten and Bruno Branco for the initial MLD experiments on TiO<sub>2</sub> nanoparticles, Willy Rook for the BET characterization, Jordi Alkemade for his support with the MLD experiments on Si wafers and ellipsometry analysis, Fatemeh Hashemi for XPS measurements, Miguel Martín Sómer for inputs on the photocatalytic methanol oxidation test, and Fabio Grillo for various scientific

discussions. Furthermore, the authors acknowledge the financial support from AstraZeneca and Health~ Holland, Top Sector Life Sciences & Health, to stimulate public–private partnerships.

## ■ REFERENCES

- (1) Caruso, F. Nanoengineering of Particle Surfaces. *Adv. Mater.* **2001**, *13*, 11–22.
- (2) Ni, B.; Wang, X. Chemistry and properties at a sub-nanometer scale. *Chemical Science* **2016**, *7*, 3978–3991.
- (3) Elam, J. W.; Routkevitch, D.; Mardilovich, P. P.; George, S. M. Conformal Coating on Ultrahigh-Aspect-Ratio Nanopores of Anodic Alumina by Atomic Layer Deposition. *Chem. Mater.* **2003**, *15*, 3507–3517.
- (4) Ni, B.; Shi, Y.; Wang, X. The Sub-Nanometer Scale as a New Focus in Nanoscience. *Adv. Mater.* **2018**, *30*, 1802031.
- (5) Lee, W. A.; Pernodet, N.; Li, B.; Lin, C. H.; Hatchwell, E.; Rafailovich, M. H. Multicomponent polymer coating to block photocatalytic activity of TiO<sub>2</sub> nanoparticles. *Chem. Commun.* **2007**, 4815.
- (6) Livraghi, S.; Corazzari, I.; Paganini, M. C.; Ceccone, G.; Giamello, E.; Fubini, B.; Fenoglio, I. Decreasing the oxidative potential of TiO<sub>2</sub> nanoparticles through modification of the surface with carbon: a new strategy for the production of safe UV filters. *Chem. Commun.* **2010**, *46*, 8478.
- (7) Morsella, M.; d'Alessandro, N.; Lanterna, A. E.; Scaiano, J. C. Improving the Sunscreen Properties of TiO<sub>2</sub> through an Understanding of Its Catalytic Properties. *ACS Omega* **2016**, *1*, 464–469.
- (8) van Driel, B.; Wezendonk, T.; van den Berg, K.; Kooyman, P.; Gascon, J.; Dik, J. Determination of early warning signs for photocatalytic degradation of titanium white oil paints by means of surface analysis. *Spectrochim. Acta, Part A* **2017**, *172*, 100–108.
- (9) Tran, D. T.; Salmon, R. Potential photocarcinogenic effects of nanoparticle sunscreens. *Australas. J. Dermatol.* **2011**, *52*, 1–6.
- (10) Guo, J.; Van Bui, H.; Valdesueiro, D.; Yuan, S.; Liang, B.; van Ommen, J. Suppressing the Photocatalytic Activity of TiO<sub>2</sub> Nanoparticles by Extremely Thin Al<sub>2</sub>O<sub>3</sub> Films Grown by Gas-Phase Deposition at Ambient Conditions. *Nanomaterials* **2018**, *8*, 61.
- (11) Guo, J.; Yuan, S.; Yu, Y.; van Ommen, J. R.; Van Bui, H.; Liang, B. Room-temperature pulsed CVD-grown SiO<sub>2</sub> protective layer on TiO<sub>2</sub> particles for photocatalytic activity suppression. *RSC Adv.* **2017**, *7*, 4547–4554.
- (12) Xiao, J.; Chen, W.; Wang, F.; Du, J. Polymer/TiO<sub>2</sub> Hybrid Nanoparticles with Highly Effective UV-Screening but Eliminated Photocatalytic Activity. *Macromolecules* **2013**, *46*, 375–383.
- (13) Morra, M.; Cassinelli, C.; Cascardo, G.; Cahalan, P.; Cahalan, L.; Fini, M.; Giardino, R. Surface engineering of titanium by collagen immobilization. Surface characterization and in vitro and in vivo studies. *Biomaterials* **2003**, *24*, 4639–4654.
- (14) Yu, W. W.; Chang, E.; Falkner, J. C.; Zhang, J.; Al-Somali, A. M.; Sayes, C. M.; Johns, J.; Drezek, R.; Colvin, V. L. Forming Biocompatible and Nonaggregated Nanocrystals in Water Using Amphiphilic Polymers. *J. Am. Chem. Soc.* **2007**, *129*, 2871–2879.
- (15) Hansen, N. M. L.; Plackett, D. Sustainable Films and Coatings from Hemicelluloses: A Review. *Biomacromolecules* **2008**, *9*, 1493–1505.
- (16) Morsella, M.; Giammatteo, M.; Arrizza, L.; Tonucci, L.; Bressan, M.; d'Alessandro, N. Lignin coating to quench photocatalytic activity of titanium dioxide nanoparticles for potential skin care applications. *RSC Adv.* **2015**, *5*, 57453–57461.
- (17) Bakalova; Zhelev, Z.; Kokuryo, D.; Spasov, L.; Aoki, I. Chemical nature and structure of organic coating of quantum dots is crucial for their application in imaging diagnostics. *Int. J. Nanomed.* **2011**, 1719.
- (18) Nakayama, N.; Hayashi, T. Preparation of TiO<sub>2</sub> nanoparticles surface-modified by both carboxylic acid and amine: Dispersibility and stabilization in organic solvents. *Colloids Surf., A* **2008**, *317*, 543–550.

- (19) Jalili, M. M.; Davoudi, K.; Zafarmand Sedigh, E.; Farrokhpay, S. Surface treatment of TiO<sub>2</sub> nanoparticles to improve dispersion in non-polar solvents. *Adv. Powder Technol.* **2016**, *27*, 2168–2174.
- (20) Yu, F.; Chen, Y.; Liang, X.; Xu, J.; Lee, C.; Liang, Q.; Tao, P.; Deng, T. Dispersion stability of thermal nanofluids. *Prog. Nat. Sci.* **2017**, *27*, 531–542.
- (21) Larson-Smith, K.; Pozzo, D. C. Pickering Emulsions Stabilized by Nanoparticle Surfactants. *Langmuir* **2012**, *28*, 11725–11732.
- (22) Krishnamoorti, R. Strategies for Dispersing Nanoparticles in Polymers. *MRS Bull.* **2007**, *32*, 341–347.
- (23) Jouet, R. J.; Warren, A. D.; Rosenberg, D. M.; Bellitto, V. J.; Park, K.; Zachariah, M. R. Surface Passivation of Bare Aluminum Nanoparticles Using Perfluoroalkyl Carboxylic Acids. *Chem. Mater.* **2005**, *17*, 2987–2996.
- (24) Hornberger, H.; Virtanen, S.; Boccaccini, A. Biomedical coatings on magnesium alloys – A review. *Acta Biomater.* **2012**, *8*, 2442–2455.
- (25) Popat, A.; Liu, J.; Lu, G. Q. M.; Qiao, S. Z. A pH-responsive drug delivery system based on chitosan coated mesoporous silica nanoparticles. *J. Mater. Chem.* **2012**, *22*, 11173.
- (26) Czok, G. S.; Werther, J. Liquid spray vs. gaseous precursor injection — Its influence on the performance of particle coating by CVD in the fluidized bed. *Powder Technol.* **2006**, *162*, 100–110.
- (27) Zasadzinski, J.; Viswanathan, R.; Madsen, L.; Garnæs, J.; Schwartz, D. Langmuir-Blodgett films. *Science* **1994**, *263*, 1726–1733.
- (28) Kubono, A.; Okui, N. Polymer thin films prepared by vapor deposition. *Prog. Polym. Sci.* **1994**, *19*, 389–438.
- (29) Sreenivasan, R.; Gleason, K. K. Overview of Strategies for the CVD of Organic Films and Functional Polymer Layers. *Chem. Vap. Deposition* **2009**, *15*, 77–90.
- (30) Chen, N.; Kim, D. H.; Kovacik, P.; Sojoudi, H.; Wang, M.; Gleason, K. K. Polymer Thin Films and Surface Modification by Chemical Vapor Deposition: Recent Progress. *Annu. Rev. Chem. Biomol. Eng.* **2016**, *7*, 373–393.
- (31) Lau, K. K.; Gleason, K. K. Particle functionalization and encapsulation by initiated chemical vapor deposition (iCVD). *Surf. Coat. Technol.* **2007**, *201*, 9189–9194.
- (32) Kubono, A.; Yuasa, N.; Shao, H.-L.; Umemoto, S.; Okui, N. In-situ study on alternating vapor deposition polymerization of alkyl polyamide with normal molecular orientation. *Thin Solid Films* **1996**, *289*, 107–111.
- (33) Zhou, H.; Bent, S. F. Fabrication of organic interfacial layers by molecular layer deposition: Present status and future opportunities. *J. Vac. Sci. Technol., A* **2013**, *31*, 040801.
- (34) Yoshimura, T.; Tatsuura, S.; Sotoyama, W. Polymer films formed with monolayer growth steps by molecular layer deposition. *Appl. Phys. Lett.* **1991**, *59*, 482–484.
- (35) Van Bui, H.; Grillo, F.; van Ommen, J. R. Atomic and molecular layer deposition: off the beaten track. *Chem. Commun.* **2017**, *53*, 45–71.
- (36) Sundberg, P.; Karppinen, M. Organic and inorganic–organic thin film structures by molecular layer deposition: A review. *Beilstein J. Nanotechnol.* **2014**, *5*, 1104–1136.
- (37) Meng, X. An overview of molecular layer deposition for organic and organic–inorganic hybrid materials: mechanisms, growth characteristics, and promising applications. *J. Mater. Chem. A* **2017**, *5*, 18326–18378.
- (38) Weimer, A. W. Particle atomic layer deposition. *J. Nanopart. Res.* **2019**, *21*, 9.
- (39) van Ommen, J. R.; Goulas, A. Atomic layer deposition on particulate materials. *Materials Today Chemistry* **2019**, *14*, 100183.
- (40) Grillo, F.; La Zara, D.; Mulder, P.; Kreutzer, M. T.; Ruud van Ommen, J. Oriented Attachment and Nanorod Formation in Atomic Layer Deposition of TiO<sub>2</sub> on Graphene Nanoplatelets. *J. Phys. Chem. C* **2018**, *122*, 19981–19991.
- (41) Zhang, D.; La Zara, D.; Quayle, M. J.; Petersson, G.; van Ommen, J. R.; Folestad, S. Nanoengineering of Crystal and Amorphous Surfaces of Pharmaceutical Particles for Biomedical Applications. *ACS Applied Bio Materials* **2019**, *2*, 1518–1530.
- (42) Valdesueiro, D.; Meesters, G.; Kreutzer, M.; van Ommen, J. R. Gas-Phase Deposition of Ultrathin Aluminium Oxide Films on Nanoparticles at Ambient Conditions. *Materials* **2015**, *8*, 1249–1263.
- (43) Martín-Sómer, M.; Benz, D.; van Ommen, J. R.; Marugán, J. Multitarget Evaluation of the Photocatalytic Activity of P25-SiO<sub>2</sub> Prepared by Atomic Layer Deposition. *Catalysts* **2020**, *10*, 450.
- (44) Adamczyk, N. M.; Dameron, A. A.; George, S. M. Molecular Layer Deposition of Poly(p-phenylene terephthalamide) Films Using Terephthaloyl Chloride and p-Phenylenediamine. *Langmuir* **2008**, *24*, 2081–2089.
- (45) Du, Y.; George, S. M. Molecular Layer Deposition of Nylon 66 Films Examined Using in Situ FTIR Spectroscopy. *J. Phys. Chem. C* **2007**, *111*, 8509–8517.
- (46) Loscutoff, P. W.; Zhou, H.; Clendenning, S. B.; Bent, S. F. Formation of Organic Nanoscale Laminates and Blends by Molecular Layer Deposition. *ACS Nano* **2010**, *4*, 331–341.
- (47) Deiana, C.; Fois, E.; Coluccia, S.; Martra, G. Surface Structure of TiO<sub>2</sub> P25 Nanoparticles: Infrared Study of Hydroxy Groups on Coordinative Defect Sites. *J. Phys. Chem. C* **2010**, *114*, 21531–21538.
- (48) Finnie, K. S.; Cassidy, D. J.; Bartlett, J. R.; Woolfrey, J. L. IR Spectroscopy of Surface Water and Hydroxyl Species on Nanocrystalline TiO<sub>2</sub> Films. *Langmuir* **2001**, *17*, 816–820.
- (49) Ivanova, T. V.; Maydannik, P. S.; Cameron, D. C. Molecular layer deposition of polyethylene terephthalate thin films. *J. Vac. Sci. Technol., A* **2012**, *30*, 01A121.
- (50) Liang, C.; Krimm, S. Infrared spectra of high polymers. *J. Mol. Spectrosc.* **1959**, *3*, 554–574.
- (51) Daniels, W. W.; Kitson, R. E. Infrared spectroscopy of polyethylene terephthalate. *J. Polym. Sci.* **1958**, *33*, 161–170.
- (52) Boerio, F. J.; Bahl, S. K.; McGraw, G. E. Vibrational analysis of polyethylene terephthalate and its deuterated derivatives. *J. Polym. Sci., Polym. Phys. Ed.* **1976**, *14*, 1029–1046.
- (53) Cole, K. C.; Aji, A.; Pellerin, É. New Insights into the Development of Ordered Structure in Poly(ethylene terephthalate) I. Results from External Reflection Infrared Spectroscopy. *Macromolecules* **2002**, *35*, 770–784.
- (54) De A. Freire, M. T.; Damant, A. P.; Castle, L.; Reyes, F. G. R. Thermal stability of polyethylene terephthalate (PET): oligomer distribution and formation of volatiles. *Packag. Technol. Sci.* **1999**, *12*, 29–36.
- (55) Mueller, R.; Kammler, H. K.; Wegner, K.; Pratsinis, S. E. OH Surface Density of SiO<sub>2</sub> and TiO<sub>2</sub> by Thermogravimetric Analysis. *Langmuir* **2003**, *19*, 160–165.
- (56) Cail, J. I.; Stepto, R. F. T. Molecular modelling of the elastic behaviour of poly(ethylene terephthalate) network chains. *Polymer* **2003**, *44*, 6077–6087.
- (57) Bergsman, D. S.; Closser, R. G.; Tassone, C. J.; Clemens, B. M.; Nordlund, D.; Bent, S. F. Effect of Backbone Chemistry on the Structure of Polyurea Films Deposited by Molecular Layer Deposition. *Chem. Mater.* **2017**, *29*, 1192–1203.
- (58) Peng, Q.; Efimenko, K.; Genzer, J.; Parsons, G. N. Oligomer Orientation in Vapor-Molecular-Layer-Deposited Alkyl-Aromatic Polyamide Films. *Langmuir* **2012**, *28*, 10464–10470.
- (59) Bergsman, D. S.; Closser, R. G.; Bent, S. F. Mechanistic Studies of Chain Termination and Monomer Absorption in Molecular Layer Deposition. *Chem. Mater.* **2018**, *30*, 5087–5097.
- (60) Cameron, D. C.; Ivanova, T. V. (Invited) Molecular Layer Deposition. *ECS Trans.* **2013**, *58*, 263–275.
- (61) Louette, P.; Bodino, F.; Pireaux, J.-J. Poly(ethylene terephthalate) (PET) XPS Reference Core Level and Energy Loss Spectra. *Surf. Sci. Spectra* **2005**, *12*, 1–5.
- (62) Zhang, J.; Nosaka, Y. Photocatalytic oxidation mechanism of methanol and the other reactants in irradiated TiO<sub>2</sub> aqueous suspension investigated by OH radical detection. *Appl. Catal., B* **2015**, *166–167*, 32–36.
- (63) Yu, J.; Li, L.; Qian, Y.; Lou, H.; Yang, D.; Qiu, X. Facile and Green Preparation of High UV-Blocking Lignin/Titanium Dioxide Nanocomposites for Developing Natural Sunscreens. *Ind. Eng. Chem. Res.* **2018**, *57*, 15740–15748.

(64) Turchi, C. S.; Ollis, D. F. Photocatalytic degradation of organic water contaminants: Mechanisms involving hydroxyl radical attack. *J. Catal.* **1990**, *122*, 178–192.

(65) Simonsen, M. E.; Li, Z.; Søgaard, E. G. Influence of the OH groups on the photocatalytic activity and photoinduced hydrophilicity of microwave assisted sol–gel TiO<sub>2</sub> film. *Appl. Surf. Sci.* **2009**, *255*, 8054–8062.

(66) Houas, A.; Lachheb, H.; Ksibi, M.; Elaloui, E.; Guillard, C.; Herrmann, J.-M. Photocatalytic degradation pathway of methylene blue in water. *Appl. Catal., B* **2001**, *31*, 145–157.

(67) Nosaka, Y.; Nosaka, A. Y. Generation and Detection of Reactive Oxygen Species in Photocatalysis. *Chem. Rev.* **2017**, *117*, 11302–11336.

(68) Zhang, J.; Nosaka, Y. Mechanism of the OH Radical Generation in Photocatalysis with TiO<sub>2</sub> of Different Crystalline Types. *J. Phys. Chem. C* **2014**, *118*, 10824–10832.

(69) Suttiponparnit, K.; Jiang, J.; Sahu, M.; Suvachittanont, S.; Charinpanitkul, T.; Biswas, P. Role of Surface Area, Primary Particle Size, and Crystal Phase on Titanium Dioxide Nanoparticle Dispersion Properties. *Nanoscale Res. Lett.* **2010**, *6*, 27.

(70) Reznickova, A.; Novotna, Z.; Kolska, Z.; Svorcik, V. Immobilization of silver nanoparticles on polyethylene terephthalate. *Nanoscale Res. Lett.* **2014**, *9*, 305.

(71) Tkavc, T.; Petrinič, I.; Luxbacher, T.; Vesel, A.; Ristić, T.; Zemljič, L. F. Influence of O<sub>2</sub> and CO<sub>2</sub> plasma treatment on the deposition of chitosan onto polyethylene terephthalate (PET) surfaces. *Int. J. Adhes. Adhes.* **2014**, *48*, 168–176.

(72) Liang, X.; Weimer, A. W. Photoactivity passivation of TiO<sub>2</sub> nanoparticles using molecular layer deposited (MLD) polymer films. *J. Nanopart. Res.* **2010**, *12*, 135–142.

(73) Chen, Y.; Zhang, B.; Gao, Z.; Chen, C.; Zhao, S.; Qin, Y. Functionalization of multiwalled carbon nanotubes with uniform polyurea coatings by molecular layer deposition. *Carbon* **2015**, *82*, 470–478.